

Article

Nanofluidic Study of Multiscale Phase Transitions and Wax Precipitation in Shale Oil Reservoirs

Zhiyong Lu ¹, Yunqiang Wan ^{2,*}, Lilong Xu ³, Dongliang Fang ¹, Hua Wu ² and Junjie Zhong ^{3,*} 

¹ Jiangnan Oilfield Branch of Sinopec Group, Wuhan 430223, China; 45963ilymf@gmail.com (Z.L.); 1802010613@s.upc.edu.cn (D.F.)

² Sinopec Shale Oil and Gas Exploration and Development Key Laboratory, Exploration and Development Research Institute, Sinopec Jiangnan Oilfield Company, Wuhan 430223, China; bz23020007@s.upc.edu.cn

³ State Key Laboratory of Deep Oil and Gas, China University of Petroleum (East China), Qingdao 266580, China; lilongxu2020@163.com

* Correspondence: wanyq.jhyt@sinopec.com (Y.W.); zhongjunjie@upc.edu.cn (J.Z.)

Abstract: During hydraulic fracturing of waxy shale oil reservoirs, the presence of fracturing fluid can influence the phase behavior of the fluid within the reservoir, and heat exchange between the fluids causes wax precipitation that impacts reservoir development. To investigate multiscale fluid phase transition and microscale flow impacted by fracturing fluid injection, this study conducted no-water phase behavior experiments, water injection wax precipitation experiments, and water-condition phase behavior experiments using a nanofluidic chip model. The results show that in the no-water phase experiment, the gasification occurred first in the large cracks, while the matrix throat was the last, and the bubble point pressure difference between the two was 12.1 MPa. The wax precipitation phenomena during fracturing fluid injection can be divided into granular wax in cracks, flake wax in cracks, and wax precipitation in the matrix throat, and the wax mainly accumulated in the microcracks and remained in the form of particles. Compared with the no-water conditions, the large cracks and matrix throat bubble point in the water conditions decreased by 6.1 MPa and 3.5 MPa, respectively, and the presence of the water phase reduced the material occupancy ratio at each pore scale. For the smallest matrix throat, the final gas occupancy ratio under the water conditions decreased from 32% to 24% in the experiment without water. This study provides valuable insight into reservoir fracture modification and guidance for the efficient development of similar reservoirs.



Citation: Lu, Z.; Wan, Y.; Xu, L.; Fang, D.; Wu, H.; Zhong, J. Nanofluidic Study of Multiscale Phase Transitions and Wax Precipitation in Shale Oil Reservoirs. *Energies* **2024**, *17*, 2415. <https://doi.org/10.3390/en17102415>

Academic Editor: Hossein Hamidi

Received: 15 April 2024

Revised: 11 May 2024

Accepted: 13 May 2024

Published: 17 May 2024



Copyright: © 2024 by the authors. Licensee MDPI, Basel, Switzerland. This article is an open access article distributed under the terms and conditions of the Creative Commons Attribution (CC BY) license (<https://creativecommons.org/licenses/by/4.0/>).

Keywords: shale oil reservoir; hydraulic fracturing; nanofluidic; phase behavior experiment; wax precipitation

1. Introduction

The demands for oil and natural gas are increasing as human society continues to develop. However, conventional oil and gas resources are becoming scarce. As a result, people are now focusing on unconventional resources, such as shale oil and gas, which have shown great potential [1–4]. Shale reservoirs are extremely dense reservoirs characterized by high heterogeneity, ultralow porosity and permeability [5–7], and abundant nanopores [8,9]. Intermolecular interaction forces between the confined fluid and the pore wall in nanoscale space become as important as intermolecular interactions within the confined fluid, and the strong solid–liquid interactions have a significant impact on the adsorption, distribution, mass transfer, and thermodynamic properties of the fluid. These interactions also cause noticeable differences in the physical properties of the fluid in both the bulk phase and nanopores [10,11].

The study of phase behavior in confined spaces has been explored extensively using experimental [12–14], analytical [15,16], and simulation methods [17–19]. Xu et al. [20] conducted a comprehensive study on the two-phase transport properties of shale gas

and water in hydrophilic and hydrophobic nanopores by combining molecular dynamics simulations and analytical modeling. Zhang et al. [21] developed a comprehensive thermodynamic model to study the phase behavior of nanopore-confined C1–C10 and C1–C4 mixtures based on pore geometry. The results show that capillarity and adsorption lead to significant deviations in the phase envelope. To study the effect of dynamic capillary pressure on two-phase flow processes, Abbasi et al. [22] proposed a hidden iteration method and implemented it. The results show that the algorithm has good convergence and, considering the dynamic capillary effect, is the key to simulating two-phase flow in porous media. Li et al. [23] proposed a two-phase flow analysis model that takes into account the presence of the water phase. The results show that the oil flow curves of the two-phase and single-phase models are both parabolic, but because of the influences of the flow space and internal water, the oil flow rate decreases. Sharma [24] studied the confined phase behavior of ethane at different pore sizes and temperatures in the ordered mesoporous material MCM-41 at the nanoscale. The results show that the capillary condensation pressure increases with an increasing pore size and temperature.

Shale oil is a complex mixture that comprises waxes, colloids, asphaltenes, aromatics, and light hydrocarbons. This intricate composition poses a significant challenge for the development of shale oil, particularly when the reservoir fluids have a high wax content [25,26]. The shale oil and gas resources of Liang2's lower submember in the Fuxing area are 656 million tons of oil and 530 billion square meters of gas, which are large-scale resources. However, the shale reservoir has a high-waxy fluid, the size difference of matrix nanopores and microfractures is large, and the characterization of the wax precipitation in the reservoir fluid during fracturing will seriously affect the reservoir development effect.

The nanofluidic chip is an emerging experimental technology that allows for the study of heat–mass transfer and physicochemical properties of fluids at the nanoscale. This technology combines semiconductor chip processing with interdisciplinary approaches. It offers precise pore processing at the nanoscale, allows for the design of flow channel structures with a high degree of freedom, enables the flexible treatment of pore surface wettability, and allows for the visual detection and manipulation of fluid states at the nanoscale [27]. It has gradually been applied in the petroleum field, in which Wang et al. applied a nanofluidic device to visualize the phase transitions of pure alkanes and alkane mixtures under nanocondensation as a means of approximating the oil/gas phase behavior in nanopore rocks [28]. Alfi et al. utilized lab-on-a-chip techniques, along with high-resolution imaging, specifically using inverse confocal microscopy equipment, to investigate the phase behavior of hydrocarbons in nanoscale capillaries, also known as nanochannels. The results of this study indicate that this method holds great potential for experimental research on phase behavior within nanoscale pores [29]. Hu et al. utilized nanofluidic technology to construct a shale micromodel to characterize salt precipitation and dissolution. This study successfully differentiated various phases ranging from 50 nm to 5 μm , allowing for the identification of the salt precipitation point and the examination of the precipitation dynamics during CO₂ injection [30].

Because of the unclear understanding of the microscopic seepage mechanism of waxy shale oil at present, conventional laboratory experimental methods cannot reveal the characteristics of continuous phase transition before and after fracturing fluid injection under the condition of a nanoconfined effect, as well as the influence of the wax precipitation on the reservoir fluid flow characteristics. This study carried out a multiscale phase behavior experiment simulation of shale oil reservoirs after fracturing reconstruction based on nanofluidic technology. The multiscale phase transition phenomenon and wax precipitation phenomenon during water injection was directly observed in the visible area of the experiment, and the influence of the existence of the water phase on the multiscale phase transition was revealed through the analysis of the experimental data. This research offers valuable insight into waxy oil reservoir fracturing, identifies potential strategies for the development of analogous shale reservoirs, and serves as a theoretical guide and reference.

2. Experimental Part

2.1. Chip Design and Preparation

According to the reservoir's physical parameters and fracture characteristics with large differences in the pore sizes and scales, the size of the matrix and pore network was determined by considering the contribution degree of the porosity. Subsequently, a chip model that aligns with the conditions of the fractured reservoir was designed and prepared. As shown in Figure 1, the white part is the matrix throat (13 nm), the yellow parts are the matrix pores (510 nm), the red area is the large crack (10 μm level), and the green areas are the microcracks (1 μm level).

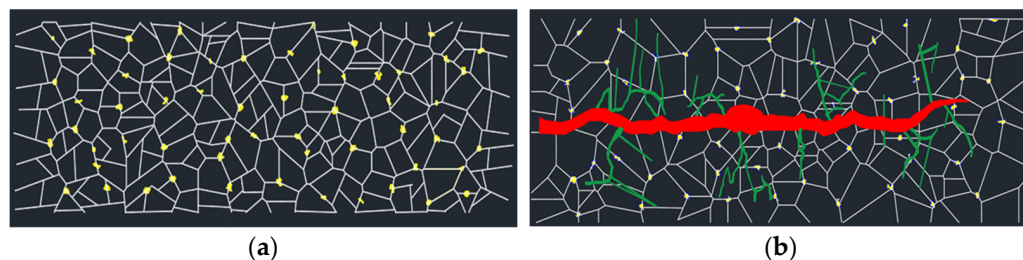


Figure 1. Chip model design. (a) The pore network model; (b) The pore-crack coupling model.

To fulfill the requirements of the nanofluidic visualization experiments, the nanochannels etched onto the chip were standardized into one-dimensional confined flow channels (specifically, channels with a one-dimensional flow channel section within the designated nanometer scale) during the chip's preparation. The whole chip production included coating and drying, exposure and development, and then the etching machine etched the developed silicon wafer; after the detection met the design requirements, the film was produced, and, finally, the full chip was obtained by anodic bonding [31,32]. The final design of the real chip model is shown in Figure 2.

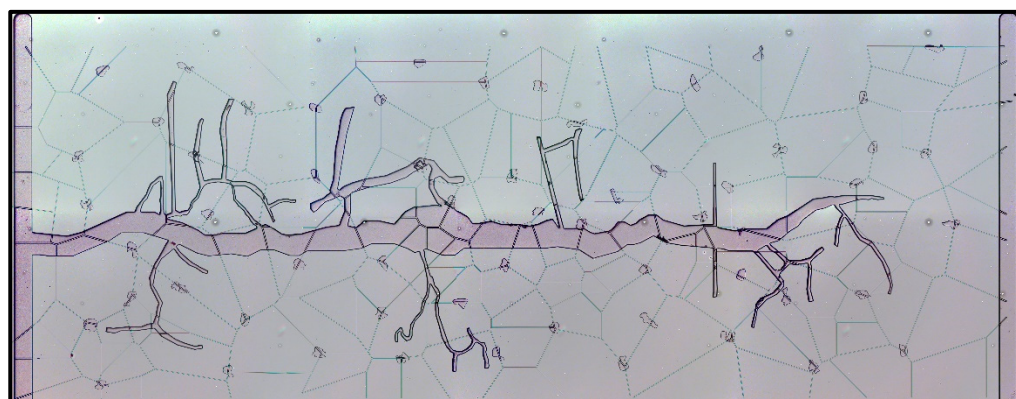


Figure 2. The actual chip models.

2.2. Experimental Materials and Equipment

The oil used in the experiment was taken from the Xingye L1HF well oil sample (Figure 3a). The fracturing fluid was purified water. Based on the chip model, this study built a flow visualization test bench, including a chip fixture, microinjection pump, pressure sensor, constant-temperature water bath, temperature sensor, microscope, and camera, according to the needs of the experiments, as shown in Figure 3b. The chip model and the experimental platform together constitute the whole system used in the conduction of the research experiment.

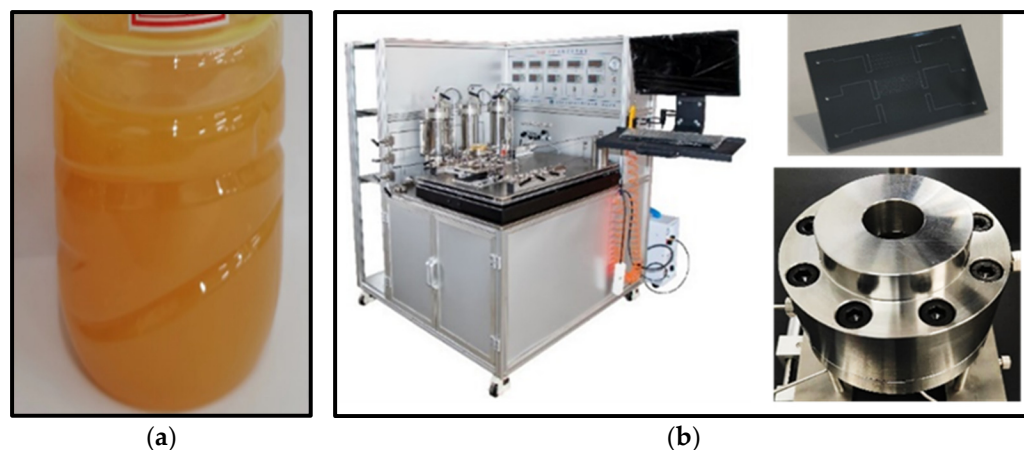


Figure 3. Images of the related equipment. (a) Experimental oil sample; (b) Experimental platform.

2.3. Experimental Scheme and Process

The experimental procedure is illustrated in Figure 4. The nanofluidic chip was affixed within a custom-made, high-temperature and high-pressure stainless-steel fixture, designed for conducting tests under elevated temperature and pressure conditions. The fixture was linked to a piston, plunger pump, and gas cylinder to facilitate fluid injection. For simulating the reservoir temperature, a water bath was connected to a hose on the fixture's side, allowing for the circulation of hot water, and the experimental temperature was monitored by inserting a thermocouple. Then, the experiment was carried out according to the following steps: (1) turn on the heating system of the nanofluidic chip stage and the intermediate container, set the experimental temperature to the reservoir temperature (70.8 °C), and vacuum the equipment for 3 h. (2) Step by step, increase the pressure to the reservoir's pressure condition (37.7 MPa) and stabilize for 24 h. (3) Gradually reduce the pressure and record the phase transition and corresponding pressure of the oil at various scales through a microscope. (4) Restore the chip pressure to the reservoir's pressure condition and the oil sample to the single phase; then, the fracturing fluid at room temperature, and continuously injection for 8 PV (pore volume). (5) Stop the injection of the fracturing fluid so that the chip can be stabilized for 24 h under the condition of the reservoir's temperature and the distribution of the oil, water, and wax at all pore scale levels can be balanced. (6) Repeat the pressure reduction operation, and observe and record the phase transition and corresponding pressures of the oil samples at various scales under water conditions through a microscope.

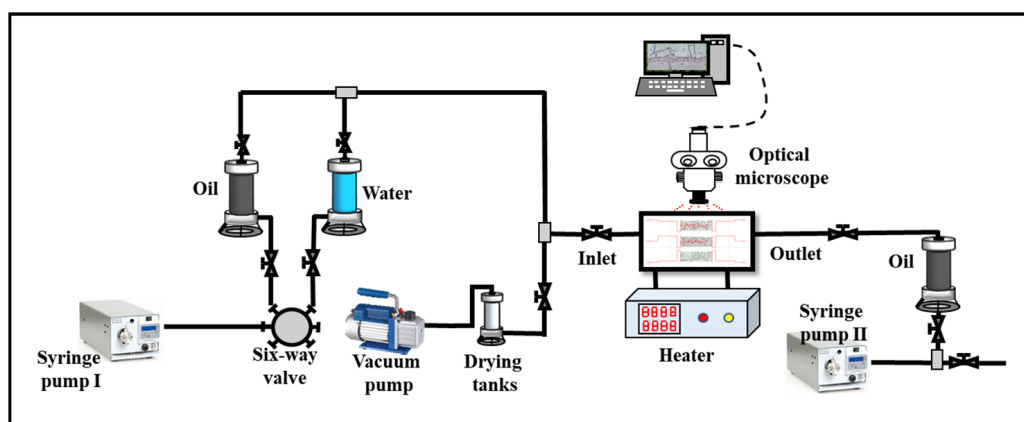


Figure 4. Experiment flowchart.

3. Results and Discussion

After the saturated oil was finished, it was found that at room temperature (25 °C), the oil sample had obvious wax precipitation characteristics, the wax showed a large range of flaked connections, and the darker the color, the more wax was precipitated. Dark-colored areas were more common in the corners of cracks and blind ends. This is because with the continuous erosion of the saturated oil, wax precipitated while being trapped to flow toward the outlet, gradually accumulating in the corners and blind ends (see Figure 5a). Because of the small size of the matrix pores and throats, the amount of wax precipitation was less, and no obvious phenomenon could be seen in the visual field. After the temperature gradually increased to the reservoir's temperature (70.8 °C), the wax in the original precipitation position gradually dissolved in the oil and disappeared from view. A relatively transparent uniform fluid appeared in the visual field, as shown in Figure 5b. It can be seen that the waxy shale oil was in a single liquid phase at the reservoir's temperature.

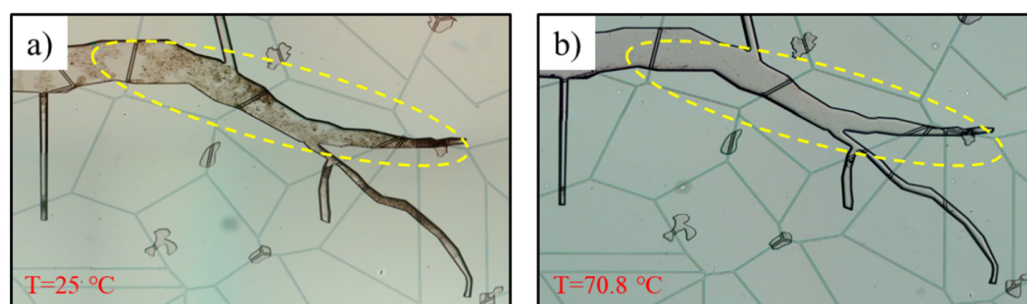


Figure 5. Wax precipitation of the waxy oil under low-temperature and reservoir-temperature conditions. (a) Wax precipitation in crack under room temperature; (b) Wax disappear under the geological temperature conditions (Yellow dashed circles indicate wax changes at corresponding locations).

3.1. Multiscale Phase Behavior Experiments under No-Water Conditions

After the oil sample in the chip reached a stable equilibrium state, the multiscale phase behavior experiment was carried out under the conditions of no water. Figure 6 shows the bubble points of various pore scales measured under a constant temperature and pressure reduction. It was found that when the pressure was reduced to 34.3 MPa, the large crack was the first to vaporize. This is due to the largest pore size of the large cracks in the chip, and when the pressure is reduced from the inlet, the pressure is transmitted more rapidly to the large cracks so that it first reaches the bubble point. However, the pore sizes of the other channels were relatively small, and they were still in the single-phase oil state due to the space limitation effect. When the pressure continued to decrease to 32.7 MPa, the bubble point was reached, and bubbles appeared in the microcracks. In the subsequent depressurizing process, the matrix pores and throat reached their respective bubble point pressures successively, which were 30.1 MPa and 22.2 MPa, respectively.

The results of the multiscale phase behavior experiments without water show that the smaller the pore size of the channel, the stronger the limiting effect and the more significant the drop in the bubble point pressure. Moreover, with the decrease in pore size, the bubble point has a greater inhibition effect. For example, the bubble point pressures of the microcracks, matrix pores, and throat decreased by 1.6 MPa, 4.2 MPa, and 12.1 MPa, respectively, compared with that of the large cracks, and the degree of reduction gradually increased.

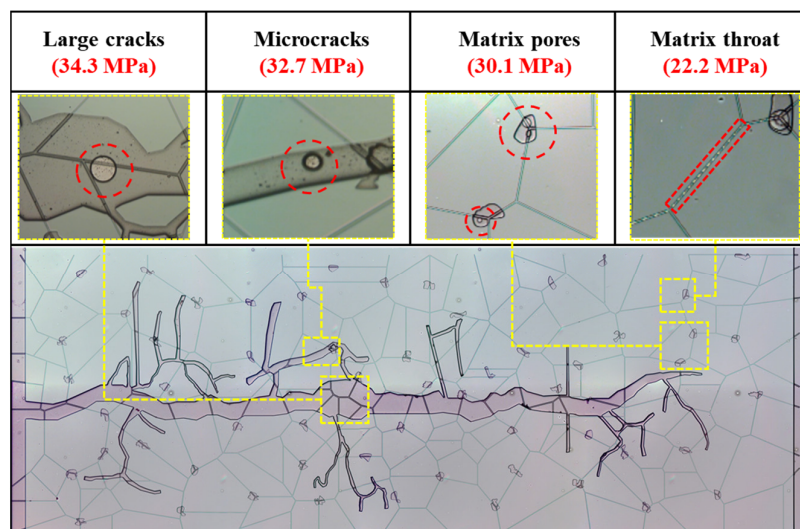


Figure 6. The bubble point pressures, at different scales, under no-water conditions (The yellow dashed box shows where the phase change occurred and enlarges the image, and the red dashed line shows where the bubble is located).

3.2. Wax Precipitation during Fracturing Fluid Injection

For the observation of the wax precipitation in the waxy oil during the fracturing fluid injection, the system's pressure was initially restored to the reservoir's pressure conditions. After recovering the oil samples to a single-phase state, water injection at room temperature was initiated to simulate the fracturing fluid injection process, with a total injection volume of 8 PV. The changes in the oil and the wax precipitation process during the fracturing fluid injection were monitored using a camera attached to an optical microscope.

In the process of injection, it was noted that wax crystals gradually developed in the field of view. This is because, with its injection, the fracturing fluid began to exchange heat with the chip and the internal fluid, the continuous injection of the fracturing fluid caused the temperature in the channel to continue to decrease, and the wax previously dissolved in the oil was reprecipitated. At the end of the injection process, the wax precipitation phenomena during the whole experiment can be divided into the following three situations: granular wax in cracks, flake wax in cracks, and wax precipitation in the nanopore throat. The injection time can also be divided into early, middle, and late injections. Figure 7 shows the wax precipitation in the reservoir at different injection volumes of fracturing fluid.

In the early stage of fracturing fluid injection (0~3 PV), the fracturing fluid first played a flooding role, and only oil–water two-phase flow could be observed in the visual field. When the fracturing fluid was injected for 1 PV, because of the small injection amount, the cooling effect of the fluid was not significant, and there was no obvious wax precipitation in the fracture channel. When the injection amount reached 2 PV, a small amount of granular wax began to precipitate and adhere to the wall surface to form a raised surface. When the fracturing fluid was injected for 3 PV, the granular wax gradually increases and accumulates, and a large amount of granular wax can be seen in the whole field of vision, with an average diameter of about 2 microns, and an obvious wax-forming interface appears at the oil–water interface at the blind end of the microfracture. This is because the dead oil at the blind end continued to exchange heat with the injected fracturing fluid, the temperature at the oil–water interface decreased significantly, and the wax could not be taken away, resulting in wax deposition.

In the middle stage of the fracturing fluid injection (4~5 PV), with the continuous erosion of the fracturing fluid, the oil content in the fracture gradually decreased, the granular wax began to migrate and further accumulate, and the flake crystals gradually formed. As can be seen from Figure 7, during the middle stage of the injection, the wax crystals were connected in sheets and showed a pattern of ups and downs on the wall. At

this time, it can be seen in the optical microscope field that different shapes of flake crystals developed in different positions of the crack.

In the late stage of the fracturing fluid injection (6~8 PV), the oil in the large cracks and microcracks was removed. With the further erosion of the fracturing fluid, part of the dead oil in the matrix pores and throat was removed, and a small amount of wax occurred in the matrix pores and throat near the fractures. In the visual field, it can be seen that flake wax precipitated from the matrix pores, but the matrix pores and throat were too small to distinguish the crystal shape of the wax phase. It can be observed that the fluid flow in the nanopore throat was less smooth than that before the fracturing fluid injection, and it can be concluded that wax was generated and seriously affected the two-phase oil–water seepage in the matrix throat.

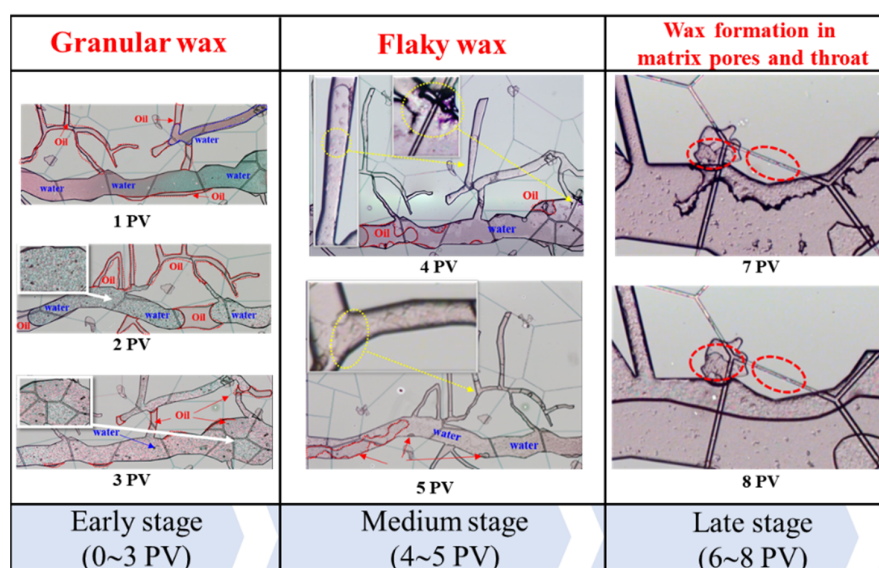


Figure 7. Wax precipitation during the fracturing fluid injection (The dashed and square boxes indicate the wax at the corresponding position).

3.3. Multiscale Phase Behavior Experiments under Water Conditions

After the observation of the wax precipitation phenomenon of the fracturing fluid injection, the injection was stopped, and the temperature was raised to stabilize the chip for 24 h under the condition of the formation temperature so that the distribution of the oil, water, and wax, at all pore scale levels, was stable and balanced. Then, the bubble point pressure, at all pore scales, under water conditions was measured by reducing the pressure again, and the phase behavior and corresponding pressure of the volatile oil, at all scales, under water conditions were observed and recorded through a microscope.

During the 24 h holding stage at the formation temperature, studies have found that the waxy flake crystals during the fracturing fluid injection stage disappeared, and some of them remained in the fracture in the form of particles and no longer melted, affecting the two-phase oil–water seepage flow and causing certain damage to the fracture conductivity. Therefore, it can be proved that for waxy shale oil, the formation of the wax precipitation phenomenon will cause cold damage to the reservoir.

The subsequent pressure reduction experiment results show that under the water conditions, the volatilization of oil still occurs first in the large fracture, and bubbles first nucleate in the water phase at the water–oil interface and then immediately jump to the oil phase to grow and expand. At this time, the bubble point pressure measured in the large fracture was 28.2 MPa, which significantly decreased by 6.1 MPa compared with that without water. When the pressure was reduced to 26.5 MPa, bubbles began to appear in the microcracks. The bubble point pressure of the microcracks was measured. Shortly after bubbles appeared in the microcracks, the bubble point pressure also reached the matrix

pores, at which time the pressure was 24.9 MPa. Finally, gas was precipitated in the matrix throat when the pressure dropped to 18.7 MPa, as shown in Figure 8.

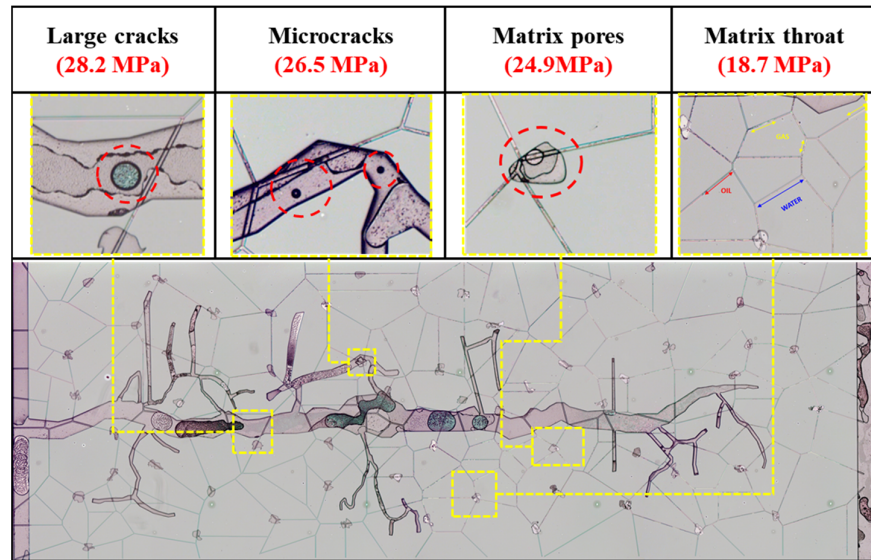


Figure 8. Bubble point pressures, at all pore scales, under water conditions (The yellow dashed box shows where the phase change occurred and enlarges the image, and the red dashed line shows where the bubble is located).

The results of the experiments under the water conditions show that the presence of fracturing fluid can significantly affect the bubble point change, at all pore scales; the presence of the water phase severely inhibits the bubble point; and the bubble point hysteresis occurs at all pore scales. As shown in Figure 9, the larger the pore scale, the more significant the impact. The bubble point pressure of the large cracks and microcracks at the micron scale decreased by about 6 MPa under the water conditions compared with the no-water conditions. The drop in the bubble point pressure in the 100 nm matrix pores was 5.2 MPa, and the drop in the bubble point pressure in the 10 nm matrix throat was only 3.5 MPa. This is also because the smaller the pore scale, the less fracturing fluid that enters, so the smaller the inhibition effect on it.

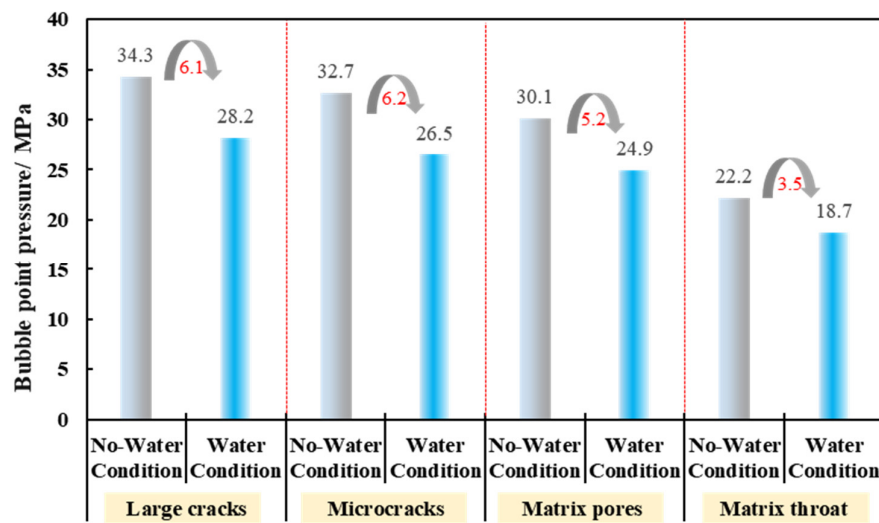


Figure 9. Comparison of the bubble point pressures, at all pore scales, under the no-water and water conditions.

3.4. Material Occupancy Ratios at Different Pore Scales

With micro-nanofluidic technology, the ratio of oil–water/oil–gas–water occupancy in the flow channels at all pore scales in the reservoir can be monitored and captured in real time. Figures 10 and 11 show the proportions of two-phase oil–water and three-phase oil–gas–water, at all pore scales, under the no-water conditions and water conditions. As can be seen in Figure 10, in the experiment at various pore scales under the conditions of no water, the gas occupancy of the large cracks was the highest, which is in line with the normal phenomenon. Because of the high bubble point pressure of the large cracks, gasification occurred first; then, the pressure gradually decreased, and the gas continued to precipitate. As can be seen in the figure, when the bubble point pressure was 34.4 MPa, the gas occupancy ratio was only 0.83%, and then it rose rapidly until the pressure dropped to 15 MPa; the increase flattened gradually, the final gas occupancy ratio reached 78.63%, and the remaining oil is only 21.37%. When the microcracks reached the bubble point, the gas occupancy ratio was 0.37%, and the final gas occupancy ratio was 56.56%. The final gas occupancy ratio of the matrix pores and throat increased to 45.54% and 32%, respectively. It also shows that with the decrease in the pore size, the smaller the gas occupancy ratio, and the more difficult it is for oil to develop in the pores.

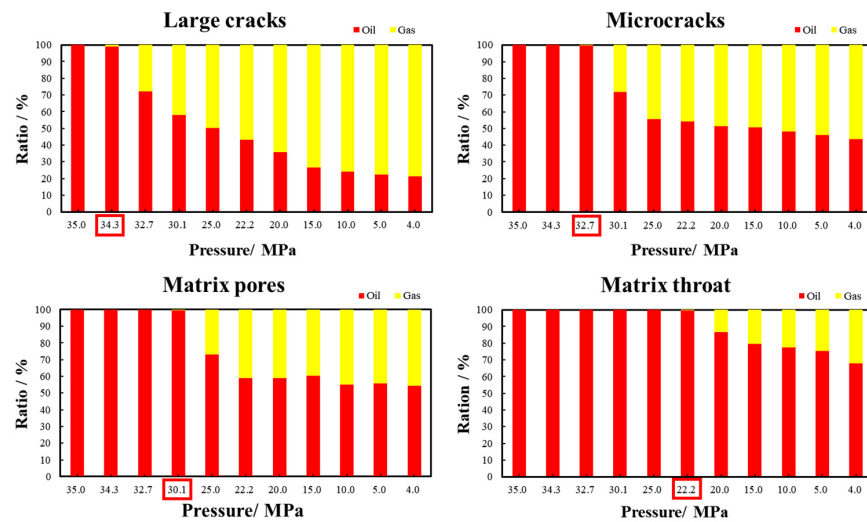


Figure 10. The ratio of oil and gas, at different pore scales, under single-phase conditions (The red box indicates the bubble point at the corresponding scale).

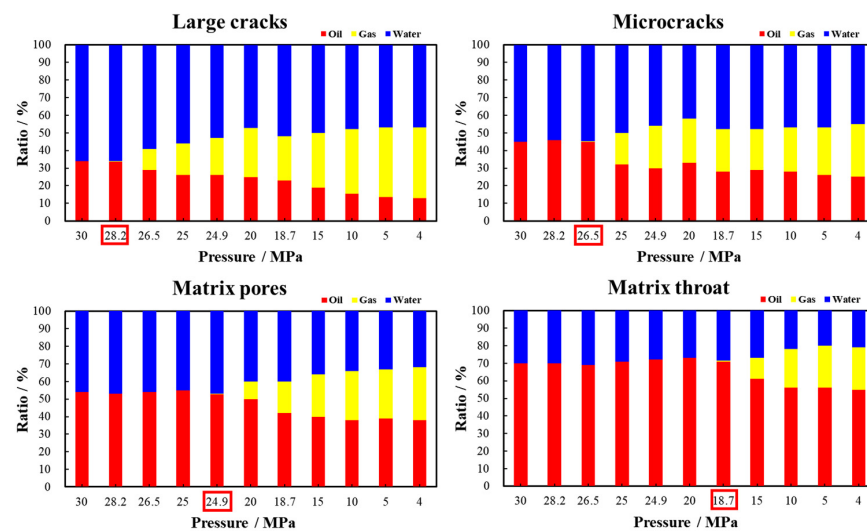


Figure 11. The ratio of oil, gas, and water, at all pore scales, under water conditions (The red box indicates the bubble point at the corresponding scale).

Figure 11 shows the occupancy ratio of the three-phase oil, gas, and water under water conditions. After large-scale fracturing fluid injection, the water phase occupancy of the large cracks reached 66%, that of microcracks was 55%, and the matrix pores and matrix throats were 46% and 30%, respectively. With the gradual reduction in the pressure, the amount of gas precipitation in the pores, at all levels, was inhibited under the water conditions. When the pressure dropped to 4 MPa, the gas occupancy ratios in the pores, at all levels, were 40%, 30%, 30%, and 24%, respectively. The corresponding final oil phase occupancy ratios were 13%, 25%, 38%, and 55%, respectively. The results show that the presence of the water phase inhibited the gas production, at all pore scales, and thus affected the degree of oil phase utilization.

To more intuitively characterize the influence under water conditions on the amount of gas precipitated, at various pore scales, this paper selected the oil–gas/oil–gas–water occupancy ratio for each pore scale under the final experimental pressure of 4 MPa for the calculations. The relative gas–oil occupancy (R_l^g) was used as an index to characterize the degassing of oil samples per unit volume.

$$R_l^g = \frac{R_g}{R_l} \quad (1)$$

where R_g is the gas phase occupancy, at all pore scales, when the pressure is 4 MPa; R_l is the oil phase occupancy, at all pore scales, when pressure is 4 MPa. The corresponding data can be directly read in Figures 10 and 11. Figure 12 shows the trend in the relative gas–oil occupancy, at all pore scales, under the following two conditions: without fracturing fluid and with fracturing fluid. It can be seen from the figure that, affected by the presence of the water phase, the relative gas–oil occupancies in the large cracks, microcracks, matrix pores, and matrix throat decreased by 0.6, 0.1, 0.05, and 0.03, respectively. The decrease was the greatest in the large cracks. It is intuitively proved that gas production, at all pore scales, will be inhibited under water conditions, and the larger the pore scale, the greater the influence of water on the gas precipitation.

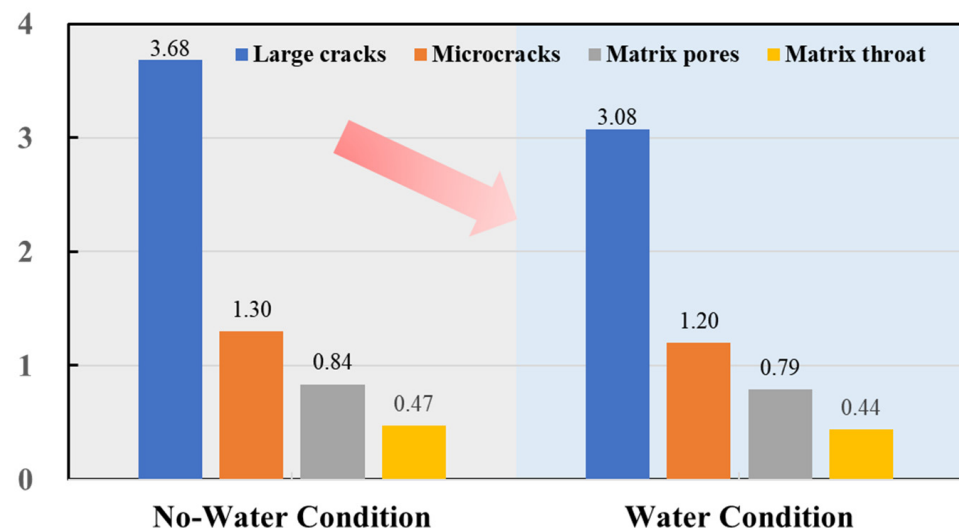


Figure 12. Comparison of the relative gas–oil occupancies, at all pore scales, under the no-water and water conditions.

4. Conclusions

In this work, this study focused on the characteristics of continuous phase transition before and after fracturing fluid injection and the impact of wax precipitation characteristics. Our findings are as follows:

- (1) In the multiscale phase behavior experiment under the no-water conditions, it was observed that gasification initiated first in the large cracks, with a corresponding bubble point pressure of 34.3 MPa. In the subsequent process with a constant temperature and pressure reduction, with the decreases in the pore size, bubble point pressure of the microcracks, matrix pores, and matrix throat were 32.7 MPa, 30.1 MPa, and 22.2 MPa, respectively.
- (2) During the process of the fracturing fluid injection, the wax precipitation phenomena manifested in the following three cases: granular wax and flake wax in the cracks, and wax formation in the matrix pores and throat. Wax precipitation was primarily concentrated in micron-sized cracks, retaining a granular form. This impeded the fluid flow and, to some extent, compromised the conductivity of the cracks.
- (3) The bubble point pressures of the different pore scales decreased further due to the influence of the water phase. The bubble point pressure of the large cracks was 28.2 MPa, representing a significant decrease of 6.1 MPa compared to the no-water conditions, the bubble points corresponding to the microcracks, matrix pores, and matrix throats decreased by 6.2 MPa, 5.2 MPa, and 3.5 MPa, respectively.
- (4) The water phase also significantly influenced the material occupancy ratios across the different pore scales. The R_l^g value intuitively proves that gas production at different pore scales will be inhibited under the water conditions, and the larger the pore scale, the greater the influence of the water on the gas precipitation.

The nanofluidic technology was used in this study to reveal the phase transition hysteresis at the multiscale and to illustrate the effects of water. The presence of the water phase would not only precipitate wax in crude oil but also affect the permeability of the pores, to a certain extent, and inhibit the bubble point at each pore scale. Also, the water phase would inhibit the gas precipitation at different pore scales. In the future development of similar waxy shale reservoirs, the impact of water can be reduced as much as possible to enhance oil recovery.

Author Contributions: Methodology, D.F.; Software, D.F.; Formal analysis, Y.W. and H.W.; Investigation, Z.L.; Data curation, Z.L. and L.X.; Writing—original draft, Z.L. and L.X.; Writing—review & editing, Y.W. and J.Z.; Supervision, Y.W. and J.Z.; Funding acquisition, J.Z. All authors have read and agreed to the published version of the manuscript.

Funding: We gratefully acknowledge the generous support from the National Natural Science Foundation of China (No. 42090024, No. 52122402 and No. 52174051), Excellent Young Scholars of Shandong Province (No. 2022HWYQ-072), and Guanghua Scholars of China University of Petroleum (East China) (No. 20210002).

Data Availability Statement: The original contributions presented in the study are included in the article, further inquiries can be directed to the corresponding author.

Conflicts of Interest: Authors Zhiyong Lu and Dongliang Fang were employed by the company Jiangnan Oilfield Branch of Sinopec Group. Authors Yunqiang Wan and Hua Wu were employed by the company Exploration and Development Research Institute Sinopec Jiangnan Oilfield Company. The remaining authors declare that the research was conducted in the absence of any commercial or financial relationships that could be construed as a potential conflict of interest.

References

1. Chauhan, A.; Salehi, F.; Jalalifar, S.; Clark, S. Two-phase modelling of the effects of pore-throat geometry on enhanced oil recovery. *Appl. Nanosci.* **2021**, *13*, 453–464. [[CrossRef](#)]
2. Jia, B.; Su, J. Advancements and Environmental Implications in Oil Shale Exploration and Processing. *Appl. Sci.* **2023**, *13*, 7657. [[CrossRef](#)]
3. Sharma, S.; Agrawal, V.; Akondi, R. Role of biogeochemistry in efficient shale oil and gas production. *Fuel* **2020**, *259*, 116247.
4. Taheri-Shakib, J.; Kantzas, A. A comprehensive review of microwave application on the oil shale: Prospects for shale oil production. *Fuel* **2021**, *305*, 121132.
5. Lee, T.; Bocquet, L.; Coasne, B. Activated desorption at heterogeneous interfaces and long-time kinetics of hydrocarbon recovery from nanoporous media. *Nat. Commun.* **2016**, *7*, 11890. [[CrossRef](#)]

6. Yang, J.; Hatcherian, J.; Hackley, P.C.; Pomerantz, A.E. Nanoscale geochemical and geomechanical characterization of organic matter in shale. *Nat. Commun.* **2017**, *8*, 2179. [[CrossRef](#)] [[PubMed](#)]
7. Falk, K.; Coasne, B.; Pellenq, R.; Ulm, F.J.; Bocquet, L. Subcontinuum mass transport of condensed hydrocarbons in nanoporous media. *Nat. Commun.* **2015**, *6*, 6949. [[CrossRef](#)] [[PubMed](#)]
8. Chen, L.; Jiang, Z.; Jiang, S.; Liu, K.; Yang, W.; Tan, J.; Gao, F. Nanopore Structure and Fractal Characteristics of Lacustrine Shale: Implications for Shale Gas Storage and Production Potential. *Nanomaterials* **2019**, *9*, 390. [[CrossRef](#)]
9. Zhang, L.; Li, B.; Jiang, S.; Xiao, D.; Lu, S.; Zhang, Y.; Chen, L. Heterogeneity characterization of the lower Silurian Longmaxi marine shale in the Pengshui area, South China. *Int. J. Coal Geol.* **2018**, *195*, 250–266. [[CrossRef](#)]
10. Sobecki, N.; Nieto-Draghi, C.; Di Lella, A.; Ding, D.Y. Phase behavior of hydrocarbons in nano-pores. *Fluid Phase Equilibria* **2019**, *497*, 104–121. [[CrossRef](#)]
11. Song, Y.; Song, Z.; Zhang, Z.; Chang, X.; Wang, D.; Hui, G. Phase Behavior of CO₂-CH₄-Water Mixtures in Shale Nanopores Considering Fluid Adsorption and Capillary Pressure. *Ind. Eng. Chem. Res.* **2022**, *61*, 5652–5660. [[CrossRef](#)]
12. Ojha, S.P.; Misra, S.; Tinni, A.; Sondergeld, C.; Rai, C. Relative permeability estimates for wolfcamp and eagle ford shale samples from oil, gas and condensate windows using adsorption-desorption measurements. *Fuel* **2017**, *208*, 52–64. [[CrossRef](#)]
13. Pini, R.; Benson, S.M. Simultaneous determination of capillary pressure and relative permeability curves from core-flooding experiments with various fluid pairs. *Water Resour. Res.* **2013**, *49*, 3516–3530. [[CrossRef](#)]
14. Liu, J.; Sheng, J.J.; Wang, X.; Ge, H.; Yao, E. Experimental study of wettability alteration and spontaneous imbibition in chinese shale oil reservoirs using anionic and nonionic surfactants. *J. Petrol. Sci. Eng.* **2019**, *175*, 624–633. [[CrossRef](#)]
15. Miqueu, C.; Grégoire, D. Estimation of pore pressure and phase transitions of water confined in nanopores with non-local density functional theory. *Mol. Phys.* **2020**, *118*, e1742935. [[CrossRef](#)]
16. Song, W.; Yao, J.; Li, Y.; Sun, H.; Wang, D.; Yan, X. Gas–water relative permeabilities fractal model in dual-wettability multiscale shale porous media during injected water spontaneous imbibition and flow back process. *Fractals* **2020**, *28*, 2050103. [[CrossRef](#)]
17. De Andrade, D.D.C.J.; Nojabaei, B. Phase Behavior and Composition Distribution of Multiphase Hydrocarbon Binary Mixtures in Heterogeneous Nanopores: A Molecular Dynamics Simulation Study. *Nanomaterials* **2021**, *11*, 2431. [[CrossRef](#)]
18. Mandal, S.; Singh, S.; Bhattacharjee, S.; Khan, S. Phase behaviour of confined associating fluid in a functionalized slit pore: A Monte Carlo study. *Fluid Phase Equilibria* **2021**, *531*, 112909. [[CrossRef](#)]
19. Zhang, T.; Javadpour, F.; Li, J.; Zhao, Y.; Zhang, L.; Li, X. Pore-scale perspective of gas/water two-phase flow in shale. *SPE J.* **2021**, *26*, 828–846. [[CrossRef](#)]
20. Xu, H.; Yu, H.; Fan, J.; Zhu, Y.; Wang, F.; Wu, H. Two-phase transport characteristic of shale gas and water through hydrophilic and hydrophobic nanopores. *Energy Fuels* **2020**, *34*, 4407–4420. [[CrossRef](#)]
21. Zhang, M.; Liu, R.; Hu, J.; Zhang, Y.; Sheng, G. A Pore-Geometry-Based Thermodynamic Model for the Nanoconfined Phase Behavior in Shale Condensate Reservoirs. *Lithosphere* **2022**, *2022*, 1989358. [[CrossRef](#)]
22. Abbasi, J.; Ghaedi, M.; Riazi, M. A new numerical approach for investigation of the effects of dynamic capillary pressure in imbibition process. *J. Pet. Sci. Eng.* **2018**, *162*, 44–54. [[CrossRef](#)]
23. Li, R.; Chen, Z.; Wu, K.; Hao, X.; Xu, J. An analytical model for water-oil two-phase flow in inorganic nanopores in shale oil reservoirs. *Pet. Sci.* **2021**, *18*, 1776–1787. [[CrossRef](#)]
24. Sharma, K.V.; Alloush, R.M.; Piri, M. Confined phase behavior of ethane in nanoporous media: An experimental investigation probing the effects of pore size and temperature. *Microporous Mesoporous Mater.* **2023**, *351*, 112459. [[CrossRef](#)]
25. Yang, F.; Dou, Z.; Xia, X.; Liu, D.; Li, C.; Yao, B.; Zhao, Y. Influence of Thermal Treating Temperature on the Performance of EVA Wax Inhibitor for Changqing Shale Oil. *Energy Fuels* **2023**, *37*, 7798–7808. [[CrossRef](#)]
26. Liu, B.; Mahlstedt, N.; Horsfield, B.; Tian, S.; Huo, Q.; Wen, Z.; Pan, Z. Phase behavior and GOR evolution using a natural maturity series of lacustrine oil-prone shale: Implications from compositional modelling. *Org. Geochem.* **2023**, *185*, 104675. [[CrossRef](#)]
27. Zhong, J.; Wang, Z.; Sun, Z.; Yao, J.; Yang, Y.; Sun, H.; Zhang, L.; Zhang, K. Research advances in microscale fluid characteristics of shale reservoirs based on nanofluidic technology. *Acta Pet. Sin.* **2023**, *44*, 207–222.
28. Wang, L.; Parsa, E.; Gao, Y.; Ok, J.T.; Neeves, K.; Yin, X.; Ozkan, E. Experimental study and modeling of the effect of nanoconfinement on hydrocarbon phase behavior in unconventional reservoirs. In Proceedings of the SPE Western North American and Rocky Mountain Joint Meeting, Denver, CO, USA, 17–18 April 2014; p. 169581.
29. Alfi, M.; Nasrabadi, H.; Banerjee, D. Experimental investigation of confinement effect on phase behavior of hexane, heptane and octane using lab-on-a-chip technology. *Fluid Phase Equilibria* **2016**, *423*, 25–33. [[CrossRef](#)]
30. Hu, X.; Wang, J.; Zhang, L.; Xiong, H.; Wang, Z.; Duan, H.; Yao, J.; Sun, H.; Zhang, L.; Song, W.; et al. Direct Visualization of Nanoscale Salt Precipitation and Dissolution Dynamics during CO₂ Injection. *Energies* **2022**, *15*, 9567. [[CrossRef](#)]
31. Zhong, J.; Zhao, Y.; Lu, C.; Xu, Y.; Jin, Z.; Mostowfi, F.; Sinton, D. Nanoscale Phase Measurement for the Shale Challenge: Multicomponent Fluids in Multiscale Volumes. *Langmuir* **2018**, *34*, 9927–9935. [[CrossRef](#)]
32. Jatukaran, A.; Zhong, J.; Persad, A.H.; Xu, Y.; Mostowfi, F.; Sinton, D. Direct Visualization of Evaporation in a Two-Dimensional Nanoporous Model for Unconventional Natural Gas. *ACS Appl. Nano Mater.* **2018**, *1*, 1332–1338. [[CrossRef](#)]

Disclaimer/Publisher’s Note: The statements, opinions and data contained in all publications are solely those of the individual author(s) and contributor(s) and not of MDPI and/or the editor(s). MDPI and/or the editor(s) disclaim responsibility for any injury to people or property resulting from any ideas, methods, instructions or products referred to in the content.